

Vortex chirality control in circular disks using dipole-coupled nanomagnets

Arabinda Haldar and A. O. Adeyeye

Citation: [Applied Physics Letters](#) **106**, 032404 (2015); doi: 10.1063/1.4906142

View online: <http://dx.doi.org/10.1063/1.4906142>

View Table of Contents: <http://scitation.aip.org/content/aip/journal/apl/106/3?ver=pdfcov>

Published by the [AIP Publishing](#)

Articles you may be interested in

[Controlling vortex chirality and polarity by geometry in magnetic nanodots](#)

Appl. Phys. Lett. **104**, 012407 (2014); 10.1063/1.4861423

[Nanomagnetic engineering of the properties of domain wall atom traps](#)

J. Appl. Phys. **110**, 123918 (2011); 10.1063/1.3671631

[Remote domain wall chirality measurement via stray field detection](#)

J. Appl. Phys. **110**, 123912 (2011); 10.1063/1.3671615

[Control of vortex chirality in regular polygonal nanomagnets using in-plane magnetic field](#)

Appl. Phys. Lett. **97**, 222503 (2010); 10.1063/1.3521407

[Vortex motion in chirality-controlled pair of magnetic disks](#)

Appl. Phys. Lett. **90**, 132501 (2007); 10.1063/1.2716861

High-Voltage Amplifiers

- Voltage Range from $\pm 50\text{V}$ to $\pm 60\text{kV}$
- Current to 25A

Electrostatic Voltmeters

- Contacting & Non-contacting
- Sensitive to 1mV
- Measure to 20kV



ENABLING RESEARCH AND
INNOVATION IN DIELECTRICS,
ELECTROSTATICS,
MATERIALS, PLASMAS AND PIEZOS



www.trekinc.com

TREK, INC. 190 Walnut Street, Lockport, NY 14094 USA • Toll Free in USA 1-800-FOR-TREK • (t):716-438-7555 • (f):716-201-1804 • sales@trekinc.com

Vortex chirality control in circular disks using dipole-coupled nanomagnets

Arabinda Haldar and A. O. Adeyeye^{a)}

Department of Electrical and Computer Engineering, National University of Singapore, 4 Engineering Drive 3, Singapore 117576, Singapore

(Received 9 October 2014; accepted 6 January 2015; published online 20 January 2015)

We report a systematic control of the chirality of circular magnetic disks where dipole field coupling drives the functionality. Our approach involves the use of two rhomboid nanomagnets with predetermined magnetization directions to bias the circular disk. Magnetostatic interaction was observed to initiate the vortex nucleation with selective chirality (clockwise or counterclockwise) when an appropriate in-plane magnetic field was applied and then removed. We have used in-field magnetic force microscopy technique to directly probe the direction of the vortex core displacements, which are sensitive to its chirality. Experimental results are in good agreement with micromagnetic simulations. © 2015 AIP Publishing LLC.

[<http://dx.doi.org/10.1063/1.4906142>]

Magnetic nanostructures are the building blocks for a wide range of non-volatile and energy efficient device technologies including magnetic quantum cellular automata (MQCA),^{1,2} neuromorphic computation,³ and high density memory.⁴ Nanomagnets (NMs) also provide excellent experimental platform for studying fundamental magnetic phenomena in confined geometries. One of the most interesting nanomagnetic structures is a magnetic vortex, which is an in-plane circulation of magnetization around a nanometer-scale central core with out-of-plane magnetization pointing either up or down.^{5,6} Circulation of the magnetization, known as vortex chirality (VC), also has two possible states depending on the sense of circulation: clockwise (CW) and counterclockwise (CCW). Magnetic vortex has shown promising applications in spin based devices such as non-volatile memory,⁷ logic,⁸ vortex based transistor,⁹ and spin wave emitter.¹⁰ Its potential for storing two units of information in a single cell lies in the fact that the polarities of the core and the VC states can be controlled independently. However, efficient and reliable switching of the core and chirality pose significant technological challenges. The core reversal has been achieved previously with electric or magnetic field pulses.^{11,12} However, the readout process for core is still a technological challenge.

Controlling chirality of the vortex is equally essential for realizing a vortex based multi-bit memory cell. Importantly, the VC can be easily readout in a conventional magnetoresistive method using a fixed reference VC.⁷ Recently, Uhlir *et al.* predicted that the VC switching can be as fast as 0.5 ns for Permalloy disk with a wedge-like asymmetry.¹³ Manipulations of VC in polygonal nanomagnets have been reported.¹⁴ However, the control of VC in circular disks was only achieved by introducing geometrical asymmetry,¹⁵ variation in the thickness,¹³ spatial field distribution,¹⁶ and coupled disks.¹⁷

In this letter, we report a simple in-plane field driven control of vortex chirality in circular disks using dipole-coupled

rhomboid NMs (R-NMs). The strategy for VC control depends on the magnetostatic interactions which lead to antiparallel orientation at remanence when initialized appropriately. In-field magnetic force microscopy (MFM) technique was employed to probe the chirality of the vortex. Experimental results were validated with micromagnetic simulations. Size and thickness dependence of vortex nucleation and annihilation in magnetization reversal have been discussed.

Arrays of polycrystalline Permalloy (Py) nanostructures were patterned on silicon dioxide substrate using high resolution electron beam lithography and lift-off techniques. Electron beam evaporation of 25 nm thick (*L*) Py was performed at 4×10^{-8} Torr base pressure and at 0.2 Å/s deposition rate on top of 5 nm Cr adhesion layer. Figure 1(a) shows the scanning electron microscopy (SEM) micrographs of the arrays of the proposed architecture where two R-NMs are placed at both sides of a disk. Arrays of standalone R-NMs and reference disks without R-NMs are shown in Figs. 1(b) and 1(c), respectively. The diameter (*D*) of the disks is 700 nm and the lateral dimensions of the R-NMs are $300 \times 150 \text{ nm}^2$. The gap (*S*) between the disks and the R-NMs was kept at 30 nm, which is small enough to have dipolar coupling. In

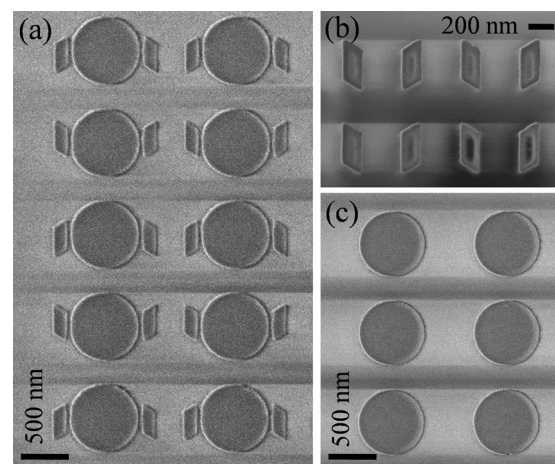


FIG. 1. SEM micrographs of the arrays of circular disks with two R-NMs (a), only R-NMs (b), and circular disks without R-NMs for reference (c).

^{a)} Author to whom correspondence should be addressed. Electronic mail: eleaao@nus.edu.sg

Figs. 1(b) and 1(c), the elements are far apart so that there is no cross talk between them. Magnetic states at remanence and in fixed field were obtained with MFM technique using commercial CoCr coated low moment tip. Conventional *lift mode* was used for obtaining magnetic contrast at a constant height and the scanning parameters were optimized experimentally. In order to improve the contrast of the vortex core, we have numerically enhanced the core region after background subtraction of the raw MFM data. In-field MFM measurements were performed by using a permanent magnet and the field was adjusted by positioning the magnet at appropriate distance.

Micromagnetic simulations were performed by solving Landau Lifshitz Gilbert equation using three dimensional “Object Oriented Micromagnetic Framework” (OOMMF) software, a public-domain code developed at NIST.¹⁸ Standard parameters for Permalloy ($\text{Ni}_{80}\text{Fe}_{20}$) were used: saturation magnetization $M_s = 8 \times 10^5$ A/m, exchange constant $A_{ex} = 1.3 \times 10^{-11}$ J/m, magnetocrystalline anisotropy $K_1 = 0$. The samples were discretized into cubes with dimensions of $5 \times 5 \times 5 \text{ nm}^3$ and this cell size is smaller than the exchange length in Permalloy. The damping coefficient was set as 0.5 for rapid convergence.

Rhomboid shaped nanomagnets were used to bias the circular disks for VC control, and its operation is shown in Fig. 2. Because of the shape anisotropy, R-NMs have unique magnetization direction at remanence after saturating them along their geometrical short axes.¹⁹ MFM images at remanence are shown in Fig. 2(a) after applying an initialization field $H_I = +2000$ Oe along $+x$ direction. Alternate bright and dark contrasts indicate up or down in-plane magnetization

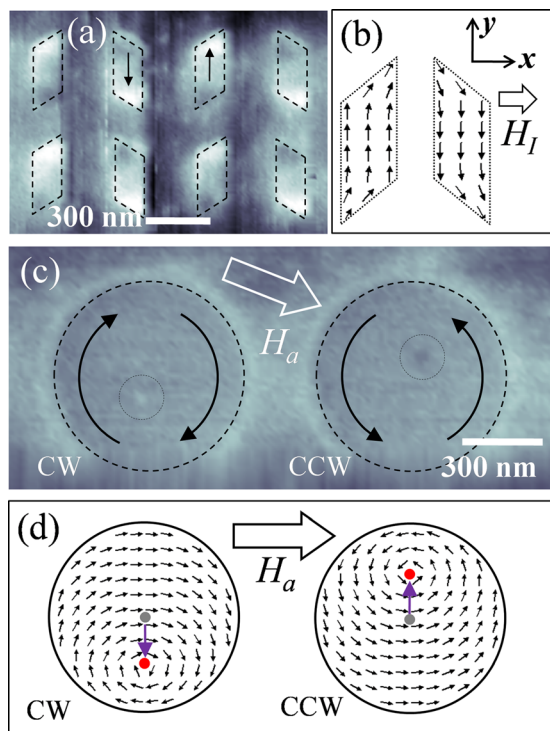


FIG. 2. (a) MFM image showing magnetization orientations in R-NMs and (b) corresponding simulation results at remanence after initialized (H_I) along the short axis. (c) MFM image taken at a fixed applied field for two circular disks showing core displacements and (d) corresponding simulation results.

directions. Figure 2(b) shows the micromagnetic mechanism of this operation with $+H_I$ and expected magnetization orientations. By comparing Fig. 2(a) and Fig. 2(b), we observed well-defined magnetic ground states in the R-NMs from the MFM images. Relative orientation of the slanted edge with respect to the external field (H_I) determines the spin orientations at remanence. Magnetization tends to align along the magnetic easy axis at much higher field during field removal process, which makes them robust and suitable for biasing operation, as their magnetic configuration does not depend on their neighbors. This is also suitable for nanomagnetic logic devices where NMs are used for biasing operation. Reversing the initialization field can flip magnetic orientations in the R-NMs.

Probing chirality using MFM technique is based on the fact that the core of the vortex moves away from the geometric center in the presence of an applied field (H_a) as a consequence of Zeeman energy minimization. Importantly, the direction of core movement is sensitive to core chirality.²⁰ This phenomenon is shown in Fig. 2(c), where the MFM image was taken in the presence of externally applied field $H_a \approx +150$ Oe. The core shifted downwards for the first disk and upwards for the other disk. We note that the cores have opposite polarities, which we do not control here. Chirality states can be explained from micromagnetic behavior, as shown in Fig. 2(d), where the core moves upward for CCW and downward for CW chirality for $+H_a$. It occurs by widening the region with magnetization along the field direction and narrowing the region with magnetization antiparallel to the applied field. With this fact, we can label CW chirality for the left disk and CCW chirality for the right disk in the MFM image, as shown in Fig. 2(c). We note that the shifted cores in the experimental MFM image are not collinear with y -axis due to misalignment of H_a from x -axis and it does not affect the mechanism. We also highlight here that the patterns were field initialized first to form the vortices prior to MFM measurements to avoid the effect of tip stray field. We rule out the possibilities of chirality switching by our low moment tip as the switching requires annihilation and subsequent nucleation of the vortex. It is noteworthy that the choice of the diameter for our disks was aimed to clearly image the displaced core of the vortex and determine the VC from that.

Vortex chirality control in an array of circular disks with two dipole-coupled R-NMs is experimentally demonstrated in Fig. 3. MFM measurements were performed in the presence of $H_a (\approx +150$ Oe) as discussed before. The results will be best understood if we only track the direction of the core displacements, which are encircled for clarity. The array in Fig. 3(a) was initialized with $H_I = -2000$ Oe $\rightarrow 0$. At remanence, the disk relaxes to a stable vortex configuration with the core at the center (not shown). The relative magnetization orientation of the two bias R-NMs was found to be opposite as predetermined by their geometries. The cores were found to move upward in the first row and downward for the second row. This implies CCW chirality for the first and CW chirality for the second row for the given direction of H_a . It also indicates that magnetizations between the biasing R-NMs and the central disk are antiparallel (see the arrows in Fig. 3(a)). The similar behavior was observed in rest of the array. We expect the results to be opposite if H_I is reversed ($H_I = +2000$ Oe $\rightarrow 0$) as compared with Fig. 3(a). This is

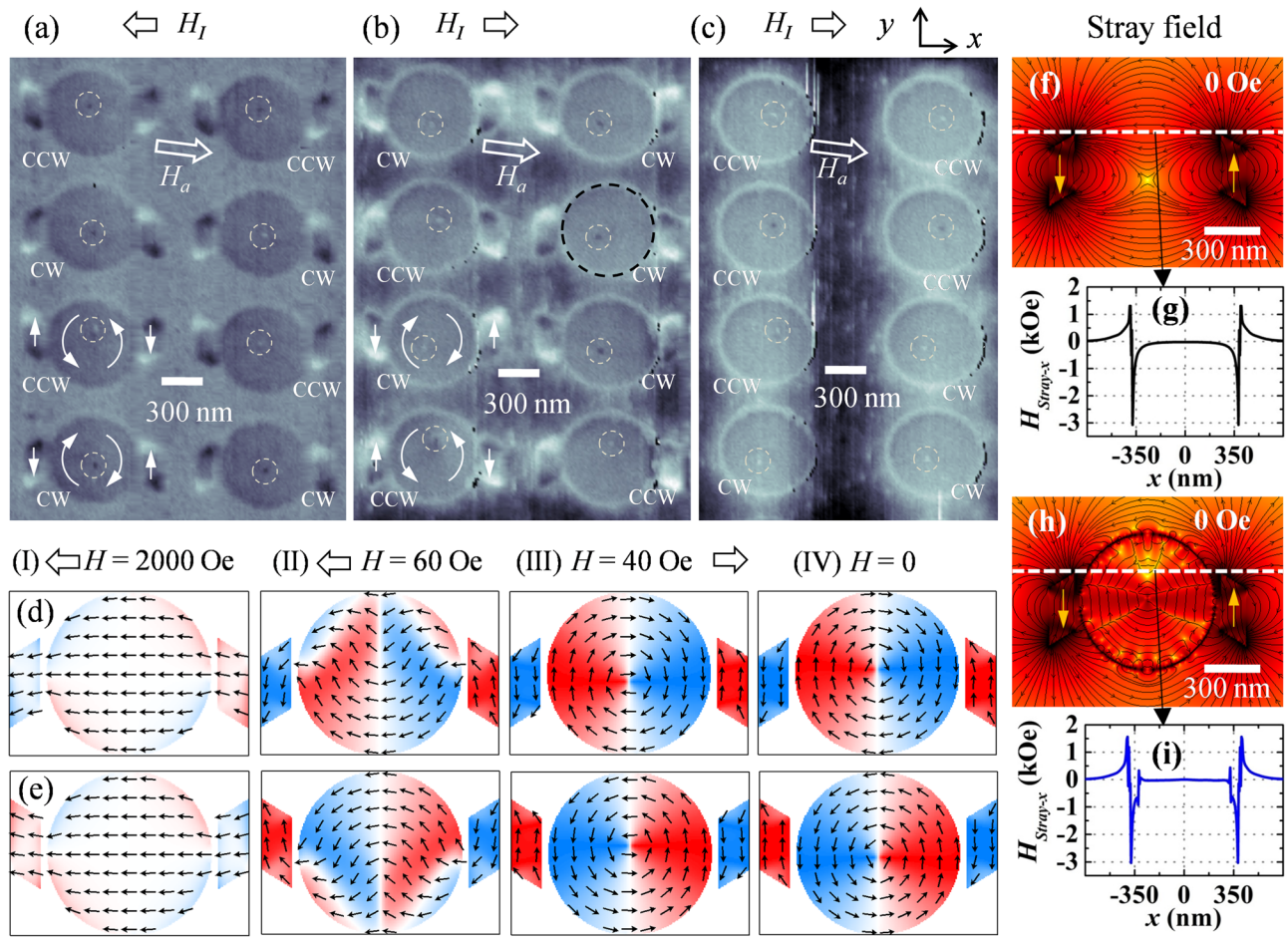


FIG. 3. MFM images obtained at a fixed applied field (H_a) after initialization with HI: $-2000 \text{ Oe} \rightarrow 0$ (a) and HI: $+2000 \text{ Oe} \rightarrow 0$ (b) for disks with R-NMs. (c) MFM image taken in a reference disk array without R-NMs with $H_I = +2000 \text{ Oe}$. Vortex cores are encircled for clarity. Micromagnetic mechanism of chirality control obtained from simulations is shown in (d) and (e). In row (d), CW chirality and row (e) CCW chirality have been shown after initialized in the $-x$ direction. Evolution of spin configurations during the initialization process is shown in steps (I)–(IV). Simulated stray fields are shown in (f)–(i). Stray field distributions at remanence from the two R-NMs are shown in (f) and a line scan of x -component of the stray field ($H_{\text{Stray-}x}$) is shown in (g). Similar data are presented in (h) and (i) for a disk with the R-NMs at remanence.

demonstrated in Fig. 3(b) where rows 1 and 3 have CW chirality and rows 2 and 4 have CCW chirality. Single faulty operation is marked with a black dotted circle. We compared these results with a disk array without bias R-NMs for reference. The results are presented in Fig. 3(c) after initializing with $H_I = +2000 \text{ Oe} \rightarrow 0$. The direction of the core shift was found to be random, which implies that the location of CW/CCW chirality is unpredictable. Therefore, controlled occurrence of CW/CCW chirality is found in the presence of dipole-coupled R-NMs in Figs. 3(a) and 3(b).

The data were reproduced several times upon reinitializing every time and then a statistical analysis was carried out on more than 100 structures. Faulty operation was found in almost 10% of the structures. In few occasions, we could not distinguish the core from the MFM contrasts. Similar studies made on reference disk sample without the R-NMs, showed that the VC distribution was random in the array and the occurrence of CW/CCW chirality had almost equal probability. This establishes the fact that our patterns does not suffer from any systematic asymmetry, which induces preferential sense of chirality as reported elsewhere.²¹ These observations confirm the reliable and robust operation of these nanostructures after taking into account the presence of fabrication defects and limitations of our VC probing method using MFM.

Figures 3(d) and 3(e) illustrate the micromagnetic mechanism of selective chirality stabilization in disks coupled to two R-NMs, as observed in Fig. 3(a). We had chosen similar dimensions in simulation as in experiment. In simulation, both the structures were initialized in the following sequence: $H_I = -2000 \text{ Oe} \rightarrow 0 \rightarrow +40 \text{ Oe} \rightarrow 0$. Saturated states are shown in step I. During the field removal process, R-NMs tend to orient to well-defined magnetic states at much higher field (-800 Oe), whereas in-homogeneous spin configuration in the disk was observed at $H = -100 \text{ Oe}$. In step II, magnetization distributions are shown with concave up for the disk in Fig. 3(d) and concave down for the disk in Fig. 3(e). It is due to the attraction of opposite magnetic charges as a consequence of magnetostatic interactions with the R-NMs. The strength of the interactions were simulated and presented in Figs. 3(f)–3(i). Distribution of the stray field from the R-NMs and the line scans clearly demonstrate the presence of the dipolar coupling. This mechanism nucleates a selective spin circulation in the disks which depends on the relative orientation of the adjacent R-NMs. Eventually, CW and CCW chiralities with shifted vortex cores were formed by reversing the field ($+40 \text{ Oe}$) to a small value (step III). Vortex retains its chirality state at remanence with the core at the center of the disk (step IV). Simulation results are

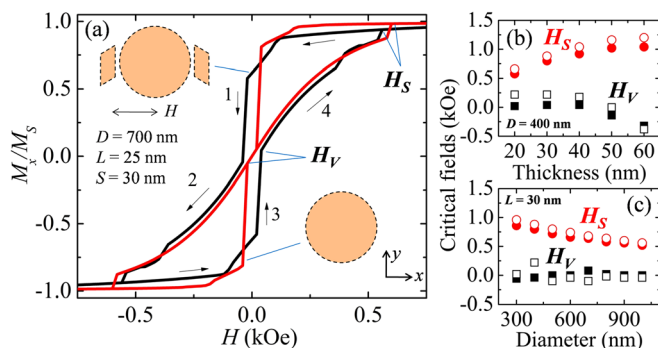


FIG. 4. (a) Comparison of simulated magnetic hysteresis loops between the circular disk with and without R-NMs. Variation of vortex nucleation (H_V) and annihilation field (H_S) as a function of (b) thickness and (c) diameter. Closed symbols represent the disks with R-NMs and open symbols refer to the reference circular disks without R-NMs.

consistent with the experimental observation in Fig. 3(a). Interestingly, the observation of antiparallel magnetization alignment of the nearest neighbor nanomagnets (bias R-NM and disk) in our structures can be used to predict the chirality of the vortex. The results in Fig. 3(b) were also reproduced in simulation (not shown). We note that we reversed the field in simulation to obtain the vortex (step III) whereas this was not required in the experiment. This difference does not affect the interpretation of the mechanism explained here.

The comparison of magnetization reversal process via nucleation/annihilation of vortex between the disks with R-NMs and without R-NMs is shown in Fig. 4(a). The similar dimensions were used as in experiment. The field where a vortex state is formed (path 3) is labeled as H_V . The field where a vortex state is annihilated and saturated with the external field (path 4) is labeled as H_S . The difference in the vortex formation and saturation fields between the disk with and without R-NMs indicates the strength of the magnetostatic interaction due to the adjacent R-NMs.

Figures 4(b) and 4(c) present the dependence of these two critical fields on the size and the thickness of the samples. For thickness variation, we had chosen a disk of diameter 400 nm (Fig. 4(b)) and for diameter variation 30 nm thick Permalloy was used (Fig. 4(c)). In disks with R-NMs, vortex formation field (H_V) decreases from 20 Oe to -320 Oe with increasing thickness of the sample from 20 nm to 60 nm, and it has insignificant variation with the diameter of the disk. On the other hand, saturation field (H_S) strongly depends on both the thickness and size of the disk. With increasing thickness of the sample from 20 nm to 60 nm, H_S increases from 580 Oe to 1040 Oe and for diameter variation in the range from 300 nm to 1000 nm, H_S decreases from 860 Oe to 520 Oe in disks with R-NMs. The corresponding values of the critical fields for a reference disk without R-NMs are shown as open symbols in Figs. 4(b) and 4(c). In general, both H_V and H_S have larger values in reference disks as compared to those of disks with R-NMs. This is attributed to the strong magnetostatic interactions in disks with R-NMs, which bias the disks locally in addition to the external field.

In summary, a simple in-plane field driven method to control of vortex chirality in sub-micron sized circular disks

using dipole-coupled rhomboid nanomagnets is presented. Magnetostatic interactions between the nearest neighbor nanomagnets (bias R-NM and disk) initiate the vortex with selective chirality when an appropriate external field applied and then removed. Anti-parallel alignment of the disk with the R-NMs was observed, which can be used to predict the VC in our structures. Experimental results were found to be in good agreement with simulations. A wide range of operation of VC control had been shown by varying the size and the thickness of the samples. This method does not alter the geometry of the circular disk to control the chirality and can be fabricated using single step lithographic process. This approach of VC control will facilitate the development of vortex based devices for information processing.

This work was supported by the National Research Foundation, Prime Minister's Office, Singapore under its Competitive Research Programme (CRP Award No. NRF-CRP 10-2012-03), SMF-NUS New Horizon Awards, and Ministry of Education, Singapore AcRF Tier 2 (Grant No. R-263-000-A19-112).

- ¹R. P. Cowburn and M. E. Welland, *Science* **287**, 1466 (2000).
- ²A. Imre, G. Csaba, L. Ji, A. Orlov, G. H. Bernstein, and W. Porod, *Science* **311**, 205 (2006).
- ³P. A. Merolla, J. V. Arthur, R. Alvarez-Icaza, A. S. Cassidy, J. Sawada, F. Akopyan, B. L. Jackson, N. Imam, C. Guo, Y. Nakamura, B. Brezzo, I. Vo, S. K. Esser, R. Appuswamy, B. Taba, A. Amir, M. D. Flickner, W. P. Risk, R. Manohar, and D. S. Modha, *Science* **345**, 668 (2014).
- ⁴D. S. Noel, A. Jayasimha, and B. Supriyo, *J. Phys. D: Appl. Phys.* **44**, 265001 (2011).
- ⁵T. Shinjo, T. Okuno, R. Hassdorf, K. Shigeto, and T. Ono, *Science* **289**, 930 (2000).
- ⁶R. P. Cowburn, D. K. Koltsov, A. O. Adeyeye, M. E. Welland, and D. M. Tricker, *Phys. Rev. Lett.* **83**, 1042 (1999).
- ⁷R. Hertel, *Nat. Nanotechnol.* **8**, 318 (2013).
- ⁸H. Jung, Y.-S. Choi, K.-S. Lee, D.-S. Han, Y.-S. Yu, M.-Y. Im, P. Fischer, and S.-K. Kim, *ACS Nano* **6**, 3712 (2012).
- ⁹D. Kumar, S. Barman, and A. Barman, *Sci. Rep.* **4**, 4108 (2014).
- ¹⁰S. Choi, K. S. Lee, K. Y. Guslienko, and S. K. Kim, *Phys. Rev. Lett.* **98**, 087205 (2007).
- ¹¹B. Van Waeyenberge, A. Puzic, H. Stoll, K. W. Chou, T. Tyliczszak, R. Hertel, M. Fahnle, H. Bruckl, K. Rott, G. Reiss, I. Neudecker, D. Weiss, C. H. Back, and G. Schutz, *Nature* **444**, 461 (2006).
- ¹²K. Yamada, S. Kasai, Y. Nakatani, K. Kobayashi, H. Kohno, A. Thiaville, and T. Ono, *Nat. Mater.* **6**, 270 (2007).
- ¹³V. Uhlig, M. Urbanek, L. Hladik, J. Spousta, M. Y. Im, P. Fischer, N. Eibagi, J. J. Kan, E. E. Fullerton, and T. Sikola, *Nat. Nanotechnol.* **8**, 341 (2013).
- ¹⁴S. Yakata, M. Miyata, S. Nonoguchi, H. Wada, and T. Kimura, *Appl. Phys. Lett.* **97**, 222503 (2010).
- ¹⁵R. K. Dumas, D. A. Gilbert, N. Eibagi, and K. Liu, *Phys. Rev. B* **83**, 060415 (2011).
- ¹⁶Y. Gaididei, D. D. Sheka, and F. G. Mertens, *Appl. Phys. Lett.* **92**, 012503 (2008).
- ¹⁷M. Natali, A. Popa, U. Ebels, Y. Chen, S. Li, and M. E. Welland, *J. Appl. Phys.* **96**, 4334 (2004).
- ¹⁸M. J. Donahue and D. G. Porter, Interagency Report NISTIR 6376, National Institute of Standards and Technology, Gaithersburg, MD, September 1999.
- ¹⁹E. Varga, M. T. Niemier, G. Csaba, G. H. Bernstein, and W. Porod, *IEEE Trans. Magn.* **49**, 4452 (2013).
- ²⁰M. Natali, I. L. Prejbeanu, A. Lebib, L. D. Buda, K. Ounadjela, and Y. Chen, *Phys. Rev. Lett.* **88**, 157203 (2002).
- ²¹M. Grimsditch, P. Vavassori, V. Novosad, V. Metlushko, H. Shima, Y. Otani, and K. Fukamichi, *Phys. Rev. B* **65**, 172419 (2002).